Korean J. Chem. Eng., 39(4), 942-953 (2022)
DOI: 10.1007/s11814-021-0975-1

pISSN: 0256-1115
eISSN: 1975-7220

Influence of Ag/Cu photodeposition on $CaTiO_3$ photocatalytic activity for degradation of Rhodamine B dye

Manjusha Passi and Bonamali Pal†

School of Chemistry and Biochemistry, Thapar Institute of Engineering & Technology, Patiala-147004, Punjab, India
(*Received 22 July 2021 • Revised 30 September 2021 • Accepted 5 October 2021*)

Abstract−The present work outlines a simple sol-gel method for the synthesis of $CaTiO_3$ (CTO) nanoparticles followed by modification with Ag, Cu via photodeposition. Different amounts (1 to 5 wt%) of Ag and Cu were loaded over CTO to form Ag/Cu-CTO nanocomposites. Several characterization techniques, such as XRD, UV-DRS, SEM, EDS, HRTEM and photoluminesence, were employed to study their structural and physicochemical properties. The photocatalytic performance of as-prepared samples was assessed by degrading Rhodamine B dye under UV irradiation. Results indicate that Ag/Cu deposition significantly enhanced the photocatalytic activity of CTO, depending upon the amount of metal loading. It found that 1 wt% Ag-CTO composite exhibited the highest (98%) photoactivity within 90 mins in contrast to 82% and 57% degradation achieved by 1 wt% Cu-CTO and bare CTO, respectively. The degradation process followed pseudo-first-order kinetics with rate constants of $k=4.5\times10^{-2}$ min^{-1} for Ag-CTO relative to $k=1.8\times10^{-2}$ min^{-1} of Cu-CTO and $k=0.86\times10^{-2}$ min^{-1} of bare. The improved photocatalytic activity was credited to the increased optical absorption and quick transfer of photoinduced electrons from $CaTiO_3$ conduction band to Ag and Cu deposits that probably retards the charge-carriers recombination as evident by their observed photoluminance behavior.

Keywords: Ag/Cu-$CaTiO_3$ Nanocomposites, Ag/Cu Cocatalysis, Photoactivity of Perovskite Nanostructures, RhB Degradation by Metal Loaded $CaTiO_3$, Calcium Titanate Photocatalysis, Ag and Cu Photodeposited $CaTiO_3$

INTRODUCTION

Global environmental problems have become more of more concern due to severe pollution, especially reacalcitrant toxic organic pollutants. For its effectiveness, simplicity, and environmentally-friendly nature, semiconductor-based photocatalysis, one of the advanced oxidation technologies, has been regarded as the most appealing method in treating waste water. It basically involves absorption of photons with energy equal to or higher than the band gap of the semiconductor to produce electron-hole pairs which then react with the oxygen and hydroxyl ions to generate active radicals that can degrade the water contaminants readily and quickly [1,2]. In this regard, a variety of semiconductor systems and their composites have been extensively developed and studied so far. Among the large assemblage of catalytic materials explored to date, perovskite oxides of the form ABO_3 are gaining huge attention because of their immense potential in diverse applications [3-5]. Owing to their remarkable physicochemical and optoelectronic properties, such as structural flexibility, electron-mobility, band gap tunability, low-cost fabrication, high thermal and photocorrosion stability, enormous efforts have been made on utilizing perovskite oxides as photocatalysts [6-8]. Recently, Calcium titanate ($CaTiO_3$), a typical titanium-containing oxide semiconductor with a perovskite-type structure has been examined in various fields including energy conversion [9-12], environmental remediation [13-15] and industrial processes [16,17]. Its unique perovskite structure offers a large platform for designing new and efficient photocatalytic materials by alteration at its A, B and O sites [18]. In addition, this n-type semiconductor even possesses conduction band potential value more negative than the benchmark photocatalyst TiO_2, making it a good substitute for the industrial catalyst TiO_2 [19,20].

Although $CaTiO_3$ is a highly photoactive material, however because of its wide bandgap and low quantum efficiency, its overall photocatalytic performance is restricted. Several factors are of relevance, but majorly two are important: ultrafast recombination of photoexcited electron-hole pairs and the limit of optical response only to UV-light [21]. Thus, the two most crucial points for achieving the high photocatalytic performance of $CaTiO_3$ are necessity to efficiently separate the photogenerated charge carriers and to expand its absorption range to the visible region. Up to now, many attempts have been made for its modification, including elemental doping [22-24], metal deposition [25,26], surface functionalization [27], heterojunction formation [28-30], and coupling with carbon materials [31-33]. Among these, depositing metal nanoparticles on semiconductors has been an important strategy to overcome these shortcomings. Generally, metal deposition on semiconductors is known to form a metal-semiconductor (M-SC) interface or Schottky barrier that furnishes an effective pathway for capturing, storing and discharging of photogenerated electrons. The contact metal actually serves as an electron trap. The Schottky barrier created at the interface permits the flow of electrons from the semiconductor to the deposited metal till the equilibration of Fermi levels. This process is influenced by nature, electronegativity, reduction potential and Fermi energy/work function of the metal [34]. Metals with

†To whom correspondence should be addressed.
E-mail: bpal@thapar.edu

lower reduction potential than CB of semiconductor ($CaTiO_3$) are a suitable choice for this.

Many literature reports reveal the significant enrichment in its photocatalytic activity by metal deposition. Recently, Shawky et al. [35] synthesized Pt-decorated $CaTiO_3$ nanocrystals with varying amounts of Pt loading and evaluated the photoreduction of nitrobenzene to aniline. The conversion rate was found to be notably improved by Pt deposition. Alzahrani et al. reported Ag(0)/$CaTiO_3$ photocatalysts with higher rates of hydrogen generation than pure $CaTiO_3$ [36]. Ag metals also show considerable antibacterial and antifungal effect. Complete deactivation of T. suecica algae was achieved in just 12 min of UV light irradiation by $CaTiO_3$ cuboids functionalized with Ag nanoparticles [37]. Au@$CaTiO_3$ nanocomposites displayed increased rates of RhB degradation under both UV and visible light irradiation [38]. Thus, it is evident that decorating metals over $CaTiO_3$ surface greatly improves its photocatalytic activity. However, only a few reports are available on its modification by Ag and Cu. Furthermore, herein we present the first report displaying the comparative effect of Ag, Cu as effective co-catalysts for $CaTiO_3$.

With this perspective, the present report deals with the preparation, characterization, and comparative study of the photocatalytic performance of series of Ag/Cu modified $CaTiO_3$ nanocomposites (with 1 to 5 wt% of Ag and Cu). Sol-gel method was applied to synthesize $CaTiO_3$ photocatalyst and then Ag and Cu were deposited onto it by the photo-deposition method. Because of their easy availability, cost-effectiveness and suitable redox potentials (Ag=0.799 V and Cu=0.337 V) [39] with respect to the conduction band of $CaTiO_3$, these metals were selected for this study. The as-synthesized samples were then characterized using various techniques and their photocatalytic performance was evaluated by removal of commercial dye rhodamine B under the illumination of UV light. The influence of loading amount of Ag and Cu on the light absorbency and photocatalytic activity was studied individually. Based on the photocatalytic results, their loading amount was optimized. A possible photocatalysis mechanism has been proposed. The main importance of this work is to study the enlargement in photocatalytic performance of wide band gap semiconductor $CaTiO_3$ with metallic Ag and Cu and to predict the superior co-catalyst among the two.

EXPERIMENTAL SECTION

1. Chemicals and Reagents

Titanium dioxide (P25-TiO_2) was obtained from Degussa Corporation, Germany. Calcium carbonate ($CaCO_3$), Cupric acetate monohydrate ($(CH_3COO)_2Cu.H_2O$), Rhodamine B dye ($C_{28}H_{31}N_2O_3Cl$), Isopropyl alcohol (C_3H_8O), ethanol (C_2H_5OH), all were acquired from Loba Chemie (India). Silver nitrate ($AgNO_3$) was purchased from Sigma-Aldrich (India). Double distilled water (D.I.) utilized during the whole study was obtained from Milli-Q (Millipore), an ultra-filtration system (conductivity=35 mho cm^{-1} at 25 °C).

2. Preparation Procedure

2-1. Preparation of $CaTiO_3$ Nanoparticles

The experimental details are presented in the flow chart of the preparation method, as shown in Scheme 1. In brief, $CaCO_3$ and

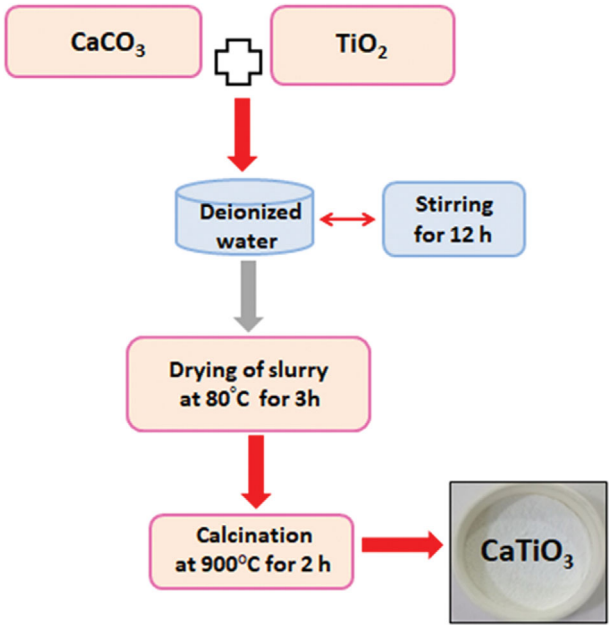

Scheme 1. Flow chart of synthesis of $CaTiO_3$ (CTO).

TiO_2 powders in equimolar ratios were mixed together in 10 ml of de-ionized (DI) water in a beaker for 30 minutes. The mixed solution was continuously stirred for 12 h at room temperature and the slurry dried in an oven at 80 °C for 3 h. The resultant dried solid was ground in a mortar pestle for 10 min until a fine and homogeneous powder was obtained and then, finally, calcined at 900 °C for 2 h, in a muffle furnace with a heating rate of 5 degree celcius/minute, yielding white-colored $CaTiO_3$ nanoparticles which were then stored in a dry container and kept in a desiccator. The as-prepared $CaTiO_3$ nanoparticles were abbreviated as (CTO).

2-2. Preparation of Ag/Cu-$CaTiO_3$ Nanocomposites by Photodeposition Method

Photodeposition of Ag and Cu on $CaTiO_3$ surface was done by the following protocol as displayed in Scheme 2. As prepared 100 mg of CTO powder was suspended in different test tubes containing distilled water and isopropyl alcohol as hole scavenger (5 ml each). The requisite amount of metal salts $AgNO_3$ (0.01 M; 928-4,636 µL) and $Cu(CH_3COO)_2{\cdot}H_2O$ (0.01 M; 1,574-7,870 µL) corresponding to different wt% (1, 3 and 5 wt%) was added to these suspension. Test tubes were then purged with argon (Ar) gas for 20 min to create an inert atmosphere and closed tightly by a rubber septum. The contents in the test tubes were photoirradiated with UV light (125 W, 10.4 mW/cm^2) for 3 h under continuous magnetic stirring in photochemical reactor. Finally, the metal deposited solutions were centrifuged (8,000 rpm), washed repeatedly with distilled water and ethanol followed by drying in oven at 70 °C for 2 h. The obtained Ag/Cu deposited nanocomposites were named as 1, 3 and 5 wt% Ag/Cu-CTO respectively.

3. Catalyst Characterization

The crystallographic studies of the prepared samples were carried out by X-ray powder diffraction PANalytical-Xpert-PRO machine equipped with a Cu-Kα radiation source (1.54 Å) operating at 45 kV with diffraction angle (2θ) ranging from 10°-80° at a scan rate of

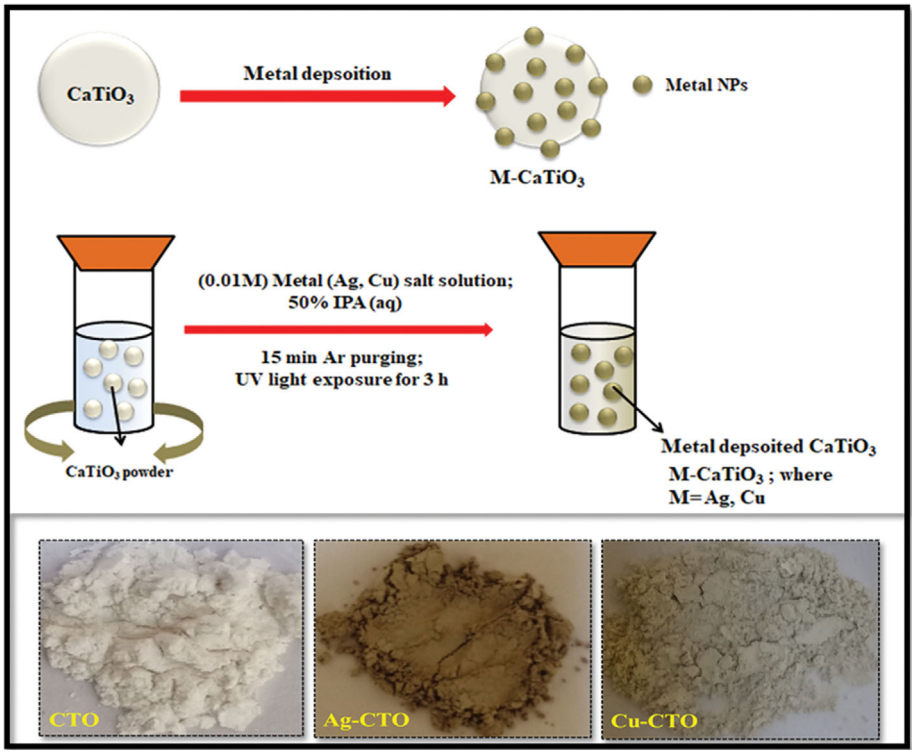

Scheme 2. Experimental procedure for photodeposition of M (M=Ag, Cu) NPs onto $CaTiO_3$.

5°/min. The optical properties were measured using a diffuse reflectance spectrophotometer (DRS, Avantes) in the region 400-900 nm, with $BaSO_4$ bar as a reference. Separation of photogenerated electron-hole pairs was examined by measuring the photoluminescence (PL) emission spectrum using a spectrofluorometer (Perkin-Elmer LS55). The shape and size analysis of the samples was done by both scanning electron microscopy (SEM;) JEOL JSM-7600F operated at 30 kV) and high-resolution transmission electron microscopy (HRTEM TALOS F200S G2 model operating at 200 kV voltage). Elemental analysis and mapping were carried out by an energy-dispersive X-ray spectrometer (EDS) linked to another SEM of the same model as mentioned above.

4. Photocatalytic Activity Study

The photocatalytic performance of the prepared samples (bare CTO, Ag/Cu-CTO) was examined by Rhodamine B (RhB) dye degradation. The photocatalytic reaction was conducted at room temperature in different test tubes. In a typical reaction, 15 mg of each catalyst was dispersed in 5 mL of 0.01 mM RhB aqueous solution. Prior to the irradiation, the suspensions were stirred in the dark for 30 min to achieve the adsorption-desorption equilibrium condition between the dye molecules and catalyst surface. Then the test tubes containing different catalysts were exposed to UV light irradiation (125 W Hg arc, 104 mW/cm^2). After definite time intervals of 15 min, the samples were withdrawn from each test tube and centrifuged at 8,000 rpm for 5 min to remove any residual solid catalyst particles. After separation, the absorbance spectra of RhB were monitored at λ_{max}=554 nm using a UV-vis spectrophotometer. As the concentration was directly proportional to the absorbance so in accordance with Beer-Lambert's law, the photodegradation efficiency was obtained using the following formula:

$$\text{Degradation rate (\%)}=(A_o-A_t)/A_o\times100=(C_o-C_t)/C_o\times100 \quad (1)$$

where, A_o, C_o denote the initial absorbance and concentration of RhB before irradiation at time '0' and A_t, C_t are the absorbance and concentration of RhB after light irradiation at time 't'.

RESULTS AND DISCUSSION

1. Structural and Morphological Properties

XRD analysis was performed to predict the crystal structure and phase composition of the as-prepared samples. Fig. 1 displays the XRD patterns of the bare and the Ag, Cu deposited $CaTiO_3$ samples for the optimum 1 wt%, respectively. Six major reflection peaks appear at diffraction angle (2θ) values of 23.23°, 33.11°, 47.49°, 59.36°, 69.48°, and 79.22°, which corresponds to the (110), (112), (220), (312), (224), (116) crystal planes of the $CaTiO_3$ structure, respectively. It can be seen that all these diffraction peaks of the CTO nanoparticles can be perfectly indexed to a perovskite-type structure well-crystallized in the orthorhombic phase with Pbnm space group (ICSD PDF# 01-078-1013), verifying that a pure single-phase was obtained. No significant diffraction peaks of Ag and Cu were witnessed, probably due to their low loading amount (1 wt%), which is consistent with previous reports [37,40]. However, a small decrease in the intensities of these peaks was observed on metal loading, which might be attributed to the suppression of the electron scattering of bare CTO upon loading of these heavy metals to its surface [41]. As the diffraction patterns of the loaded samples almost coincide with the bare CTO, this also gives indication of

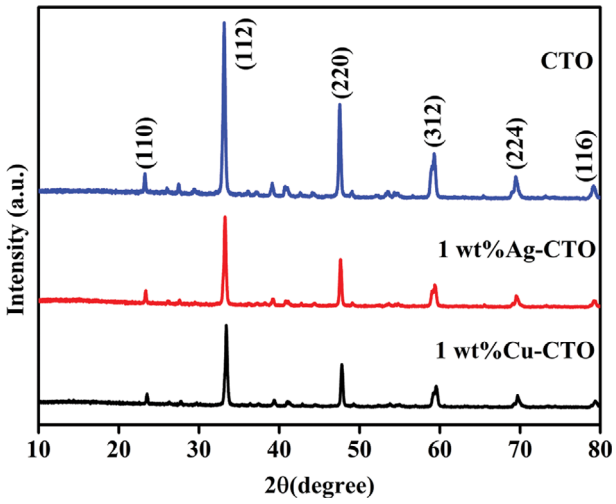

Fig. 1. X-ray diffraction patterns of different photocatalysts.

homogeneous dispersion of Ag and Cu on CTO surface.

The surface morphology of the catalysts was identified by SEM. Fig. 2(a)-(c) displays the SEM images of bare CTO and optimum 1 wt%Ag/Cu-CTO composites. Mostly spherical aggregates or clusters were obtained for all the samples. Appearance of agglomerates may be due to the high calcination temperature of 900 °C. The deposited Ag, Cu nanoparticles and the bare CTO could not be differentiated by SEM due to low resolution of the instrument. But the elemental composition and mapping results confirm their presence on CTO surface. EDS study was used for determining the quantity of various elements present in the composites. Fig. 2(a)-(c) shows their respective EDS spectra along with tables indicating the elemental content values. The expected loading amount was 1 wt% of Ag and Cu, but the observed values were 0.68% and 0.64%. The lower amount of Ag, Cu content might be due to selective area selection for EDX or because of some mass loss occurred either during the photodeposition process or by the washing procedure. In addition with all the necessary elements like (Ca, Ti, O, Ag, Cu), one additional signal of element carbon (C) was detected in all the samples that could have come from the carbon tape employed in SEM-EDX analysis to attach samples to sample holders, or maybe because of the presence of some carbonate traces. The mapping results of Ag/Cu-CTO samples along with the corresponding image are shown in Fig. 3. The dot pattern of 1 wt% Ag-CTO sample {Fig. 3(a)-(d)} clearly shows the presence of elements Ca, Ti, O, Ag appearing in green, blue, yellow and pink colors, respectively. Similar confirmation of elements, most importantly the presence of Cu, was also detected in the dot pattern of 1 wt% Cu-CTO nanocomposite {Fig. 3(e)-(h)}.

Further, the clear morphologies as well as the way of distribution of Ag and Cu nanoparticles on $CaTiO_3$ surface were elucidated

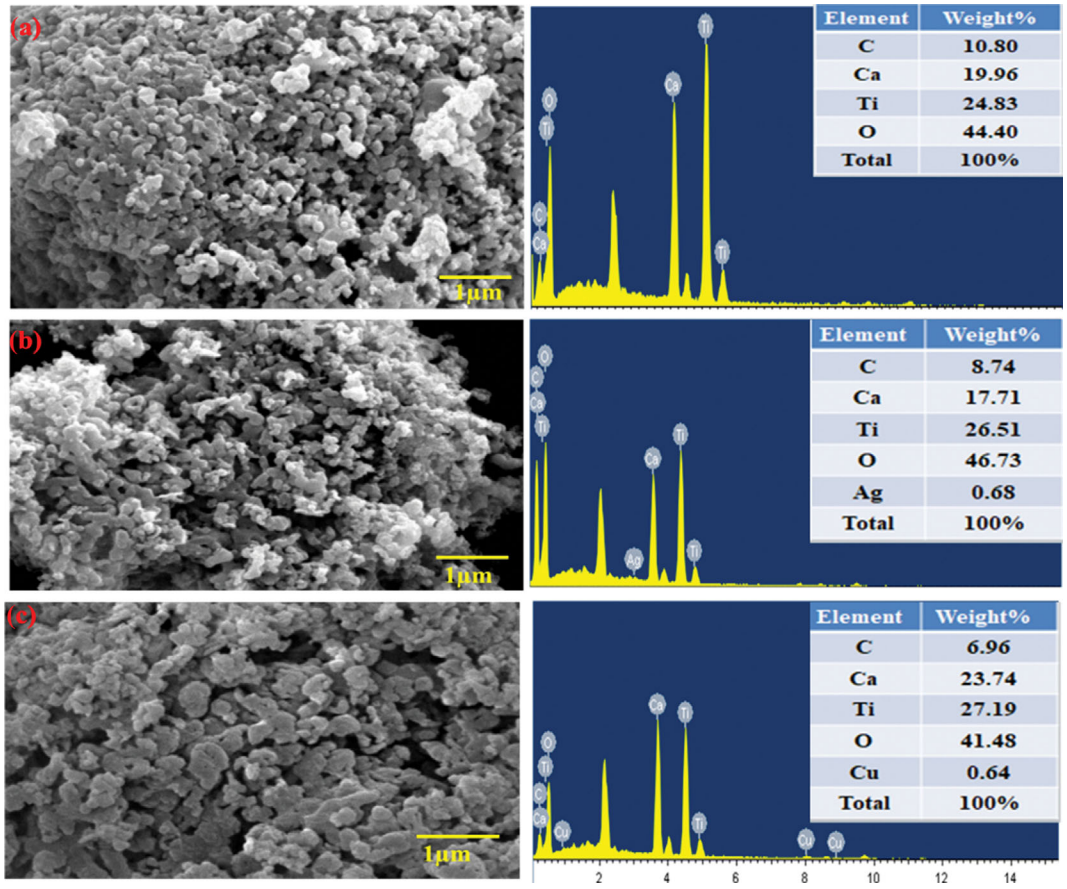

Fig. 2. SEM images of (a) bare CTO, (b) 1 wt% Ag-CTO, (c) 1 wt% Cu-CTO and their corresponding EDX profiles.

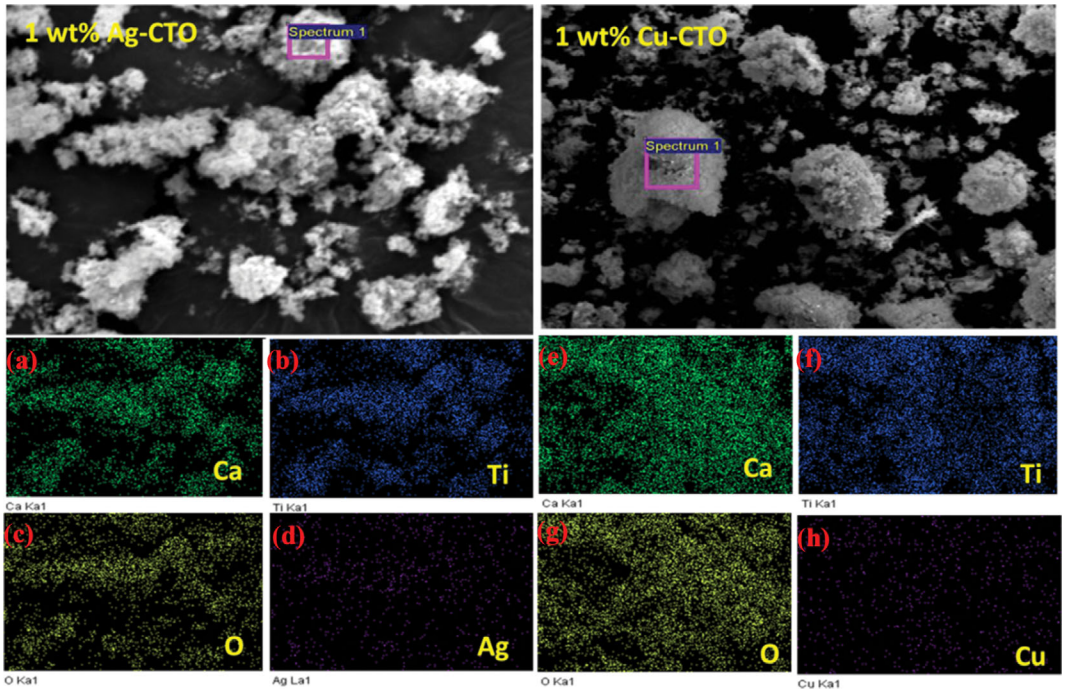

Fig. 3. Elemental dot mapping of different elements present in (a)-(d) 1 wt% Ag-CTO and (e)-(h) 1 wt% Cu-CTO photocatalysts.

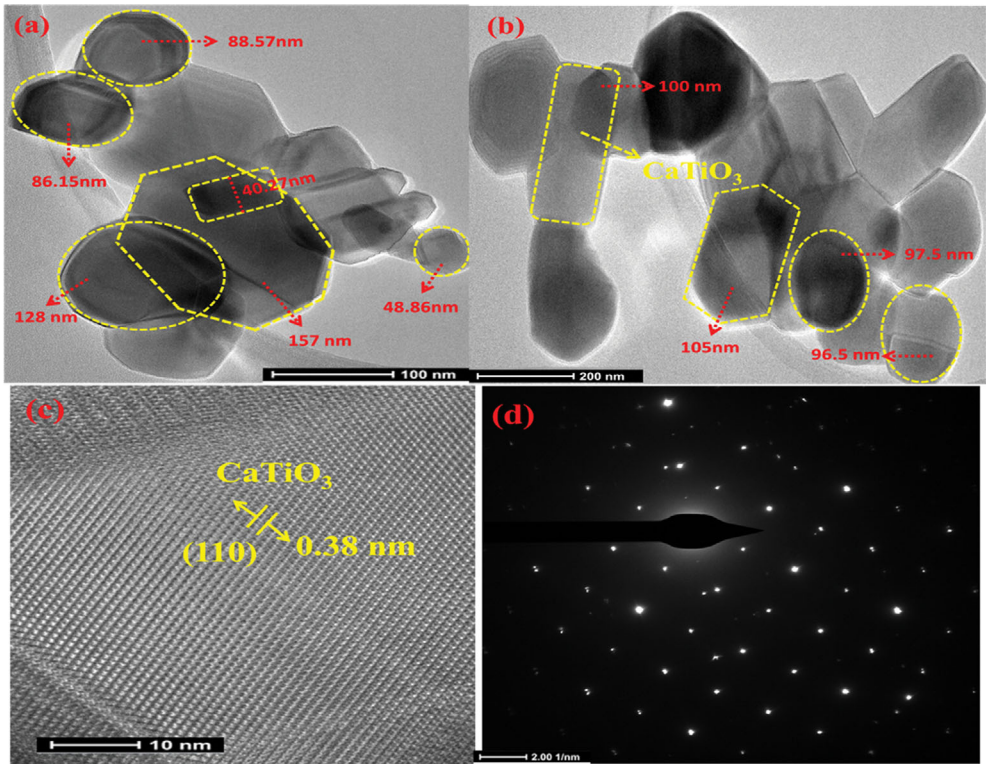

Fig. 4. HRTEM morphology (a), (b), lattice fringes (c) and SAED pattern (d) of bare $CaTiO_3$.

from their TEM and HRTEM images. The TEM images of bare CTO (Figs. 4(a) and (b)) show mixed morphological characteristics. Most of the nanoparticles attained spherical shape, while variable morphologies, such as rectangular, hexagonal and cubical, were also observed. Size of the CTO particles was measured and found to be in the range of 40-150 nm. Occurrence of large sized particles could be related to the consequence of high calcination temperature, which causes growth of the crystal. Fig. 4(c), displays

the high resolution TEM image of bare CTO, which represents clear lattice fringes of CTO with an interplanar 'd' spacing of 0.38 nm coinciding with the (110) crystal plane of pure perovskite phase CTO [42]. Fig. 5(a) and (b) represent the TEM images of 1 wt% Ag-CTO nanocomposite. Many smaller spherical Ag nanoparticles (marked by red arrows) of average size 6-12 nm were found to be uniformly deposited on the CTO surface in the form of nanodots. Its HRTEM image displayed in Fig. 5(c) further confirms the presence of Ag. The interplanar spacing (d) of 0.23 nm [43] and 0.38 nm shows the presence of (111) plane of Ag nanoparticles

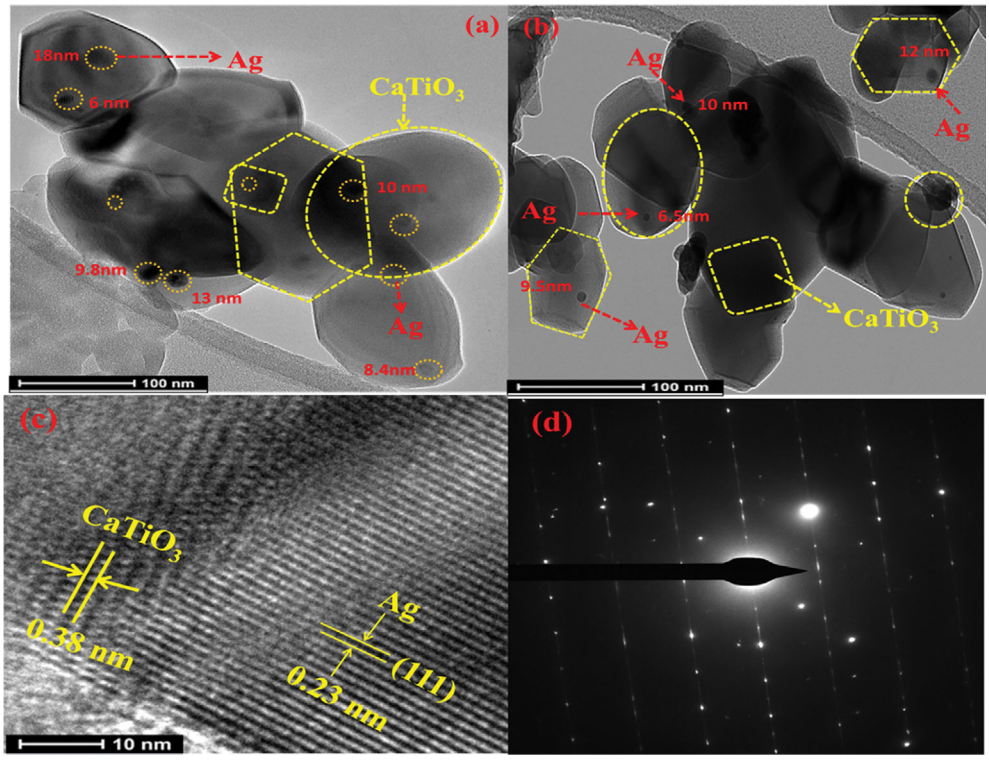

Fig. 5. HRTEM morphology (a), (b), lattice fringes (c) and SAED pattern (d) of optimum 1 wt% Ag-$CaTiO_3$ nanocomposite.

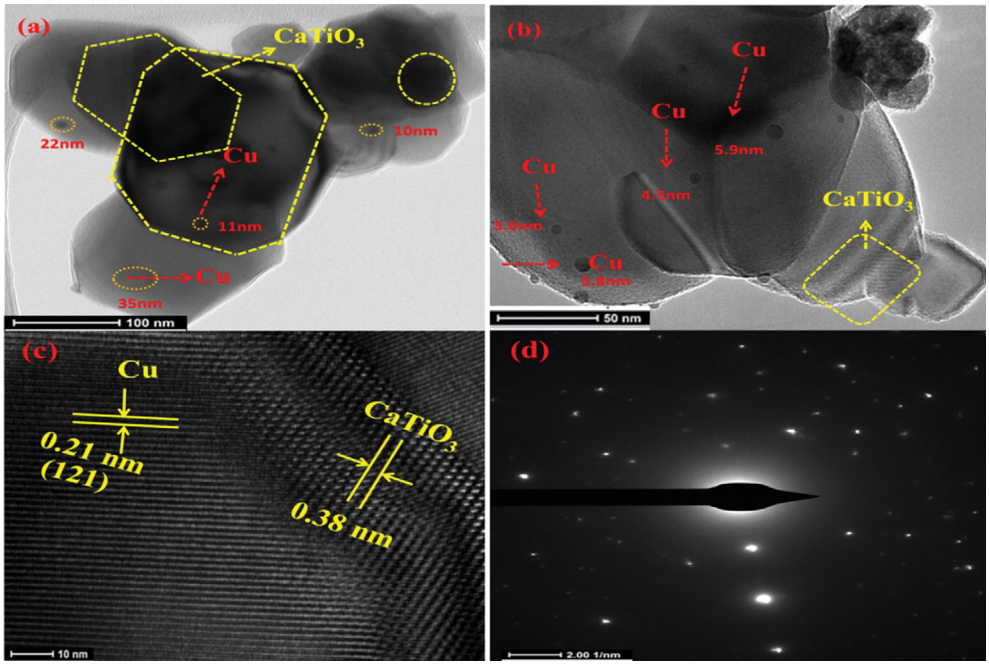

Fig. 6. HRTEM morphology (a), (b), lattice fringes (c) and SAED pattern (d) of optimum 1 wt% Cu-$CaTiO_3$ nanocomposite.

[30] anchored on (110) plane of CTO surface, respectively. Similar kinds of TEM and HRTEM images were also obtained in case of 1 wt% Cu-CTO nanocomposite as presented in Fig. 6(a)-(c). Cu nanodots of average sizes 3 to 20 nm were found to be anchored on CTO surface. Distinct fringes were also observed for Cu and CTO, where spacing 'd' of 0.21 and 0.38 nm was attributed to (121) plane of Cu [44] and (110) plane of CTO. Such results indicate the deposition of Ag and Cu nanoparticles on $CaTiO_3$ perovskite. Moreover, SAED pattern of these samples was also analyzed as shown in Figs. 4(d), 5(d) and 6(d). A series of bright spots were observed in contrast to ring pattern. The typical spot pattern reveals the high crystallinity of all the prepared samples.

Fig. 7 presents the results of ultraviolet-visible spectra of bare and 1, 3, 5 wt% Ag/Cu-CTO nanocomposites. A characteristic peak of CTO was observed at 370 nm in a UV region which could be due to the electronic transition from the valence band to the conduction band. After deposition of Ag and Cu, the absorption range of the composites was found to be significantly shifted towards the visible-light region. The typical surface plasmon resonance bands of Ag and Cu in the composites were seen in the range of 480 and 700 nm, respectively. Moreover, with the increase in their amount from 1 to 5 wt% the intensity of these plasmon bands was also found to increase gradually. Accordingly, the existence of UV as well as visible absorbance maxima in case of Ag/Cu-CTO composites clearly indicates that the material turns out to be highly photoactive, with ability to be able to respond in full range spectrum. After depositing these metals on CTO surface, the colors of the samples were also found to be changed (as inserted in Scheme 2) from the typical white color of CTO to light brown and grey in the case of Ag and Cu-CTO, respectively. This further confirms the change in the light absorption capacity of CTO by the deposited metals.

Further, the band gap energies of the samples were estimated by the use of Tauc relation [39], given by:

$$\alpha h\nu = A\,(h\nu - E_g)^n \quad (2)$$

where α=absorption coefficient, $h\nu$=photon energy, A=constant, E_g=is the band gap of the material and n is the exponent coefficient (n=1/2 for $CaTiO_3$). The exact band gap values (listed in Table 1) were calculated by plotting the graph between $(\alpha h\nu)^{1/2}$ versus the $h\nu$ as displayed in supporting information (Fig. S1(a) and (b)). Results revealed that the band gap energy values of all the prepared catalysts were lower than bare CTO (2.99 eV). The reduction in the band gap upon modification with Ag and Cu was attributed to decrease in the extent of recombination of photogenerated charge carriers. However, it was also noticed that this band gap lowering occurred only up to 3 wt%; further increasing the loading amount of Ag and Cu to 5 wt%, increases the band gap. This could be due to excessive loading of metal nanoparticles which acts as recombination centers and affects the band gap. The maximum decrease in the band gap of 2.90 eV was observed in case of 3 wt%Ag-CTO sample.

Photoluminescence (PL) spectroscopy was used to examine the extent of charge carrier separation in various samples. It is well reported that the PL intensity is directly proportional to the recombination rate of electron-hole pairs, i.e., the higher the extent of recombination, the more intense is the PL signal, and vice-versa [45]. Fig. 8 shows the room temperature PL spectra of bare and Ag/Cu-CTO nanocomposites with excitation wavelength of 370 nm. Several peaks at 423, 486 and 530 nm were obtained for all the samples. The peak at 423 nm is ascribed to near band edge emission (NBE) and the latter peaks at 486 and 530 nm defined as deep

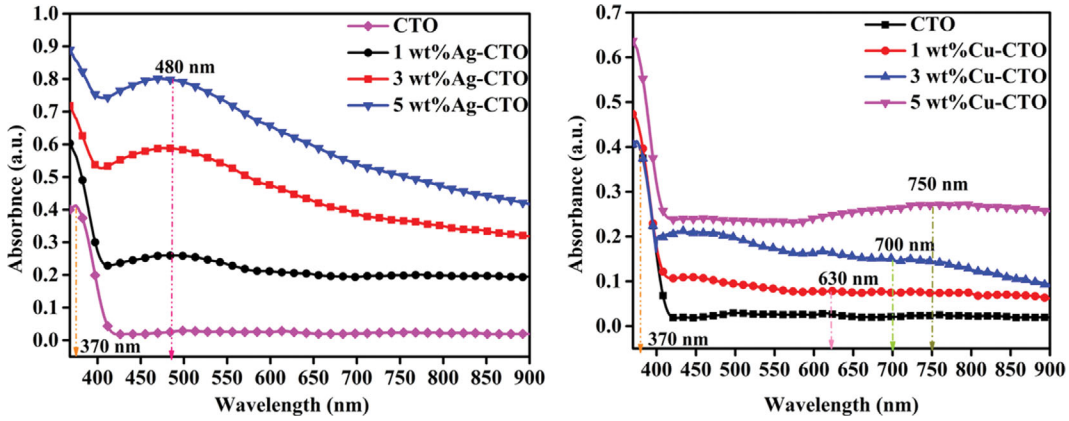

Fig. 7. Diffused reflectance spectra of various Ag and Cu loaded CTO nanocomposites.

Table 1. The absorption peaks and band gap values for bare CTO and various (1, 3 and 5 wt%) Ag/Cu-CTO nanocomposites

	Ag-CTO		Cu-CTO	
Metal content	λ_{max} (nm)	Band gap (eV)	λ_{max} (nm)	Band gap (eV)
1 wt%	480	2.91	630	2.96
3 wt%	480	2.90	730	2.95
5 wt%	480	2.94	750	2.98

level emissions (DLE). The NBE emission peak mainly centered in the UV region originates due to recombination of charge carriers formed upon excitation by radiation with energy equal to or greater than the bandgap energy. The other two deep level emissions centered in the visible region would be the result of intrinsic defects such as oxygen vacancies (V_O), Ti vacancies (V_{Ti}) or surface defects. The deposition of Ag and Cu, however, did not change much the position of band edges but resulted in significant quenching of PL intensity in comparison to the intensity of bare CTO, indicating suppression in the recombination rate of photoinduced electron-hole pairs in Ag/Cu-CTO composites. This could be credited to the electron trapping ability of Ag and Cu leading to efficient transfer of charges from CTO surface to these islands, which strongly hinders the recombination process and in turn prolongs the lifetime

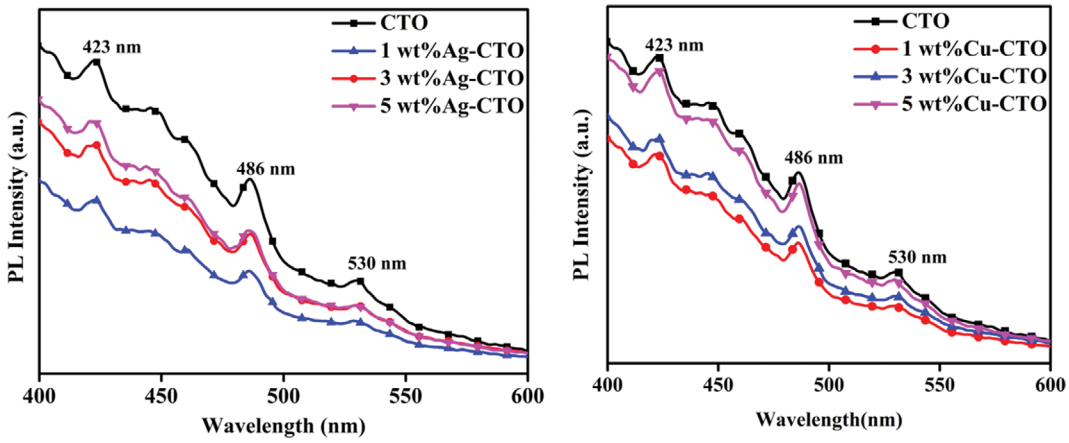

Fig. 8. Photoluminescence (λ_{max}=370 nm) spectra of various nanocomposites.

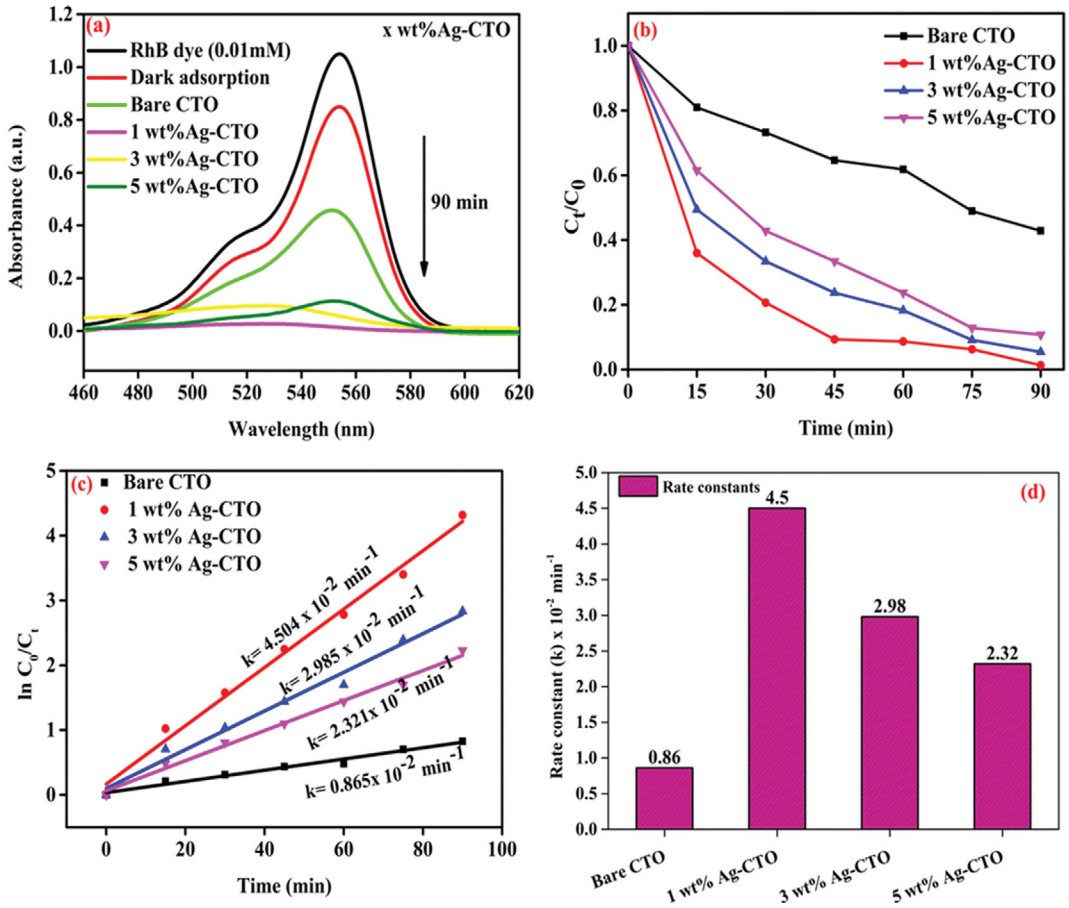

Fig. 9. (a) Comparative changes in absorption spectra of RhB dye degradation by different Ag- CTO catalysts after 90 min UV irradiation, ((b) and (c)) time course-kinetic plot, (d) their relative rate constants (k).

of charge carriers. Besides, it was observed that the highest PL quenching happens in case of 1 wt% amount of Ag/Cu-CTO nanocomposites, which implies that there is an optimal value for the quantity of metal (Ag, Cu) in order to obtain the adequate electron transportation. On further increasing the metal content beyond 1 wt%, the PL emission shows a rise in intensity due to high electron-hole recombination rate. This might be due to excessive metal deposition which can cover the CTO surface, eventually leading to decrease in the concentration of photoexcited charge carriers and also the photocatalytic activity of composites. Among all the samples, the most depressed PL signal was obtained in case of 1 wt% Ag loaded CTO.

INFLUENCE OF COINAGE METAL Ag AND Cu DEPOSITION ON $CaTiO_3$ PHOTOCATALYTIC ACTIVITY

1. Photocatalytic Activity of Ag-$CaTiO_3$

The UV-visible absorption spectra Fig. 9(a) show comparative change in absorbance of RhB dye after its photodegradation by bare and different Ag-loaded CTO nanocomposites under 90 min UV irradiation. It can be seen that absorption intensity is decreased to a varied extent depending on the amount of Ag (1 to 5 wt%) deposition, signifying the differences in RhB photodegradation efficiency among various catalysts. Definitely, Ag loading notably improved the photoactivity of CTO, and 1 wt% Ag deposition exhibits maximum catalytic activity and thereby decreased on further (3 to 5 wt%) loading. To further confirm the optimum amount of Ag loading on CTO for RhB degradation, the time course (Fig. 9(b)) plot and kinetic graphs (Fig. 9(c)) were studied and found that the photodegradation process follows pseudo-first-order rate law in all cases. Fig. 9(d) representing the histogram shows comparative reaction rate constant values. Out of various Ag loaded catalysts, the maximum rate constant (4.50×10^{-2}) was obtained in case of 1 wt% Ag loaded CTO sample under similar experimental condition.

2. Photocatalytic Activity of Cu-$CaTiO_3$

Similar results were obtained for various amounts of Cu-loaded CTO for RhB dye photodegradation as shown in Fig. 10. The changes in the absorption spectral intensity, time course plot and kinetic rate law are also varying depending upon the amount of Cu loaded on CTO as displayed in Fig. 10(a)-(c). The photocatalytic activity of Cu-CTO catalysts are seen to follow the same trend as observed by Ag loaded catalysts where 1 wt%Cu loading also exhibited the best photoactivity (1.80×10^{-2}) for RhB degradation as evident in Fig. 10(d) histogram.

The experimental result suggests that degradation ability of $CaTiO_3$ gets remarkably enhanced by depositing Ag and Cu on its surface. These metal deposits behave like electron accumulation sites and effectively trap the photo-excited electrons from CTO

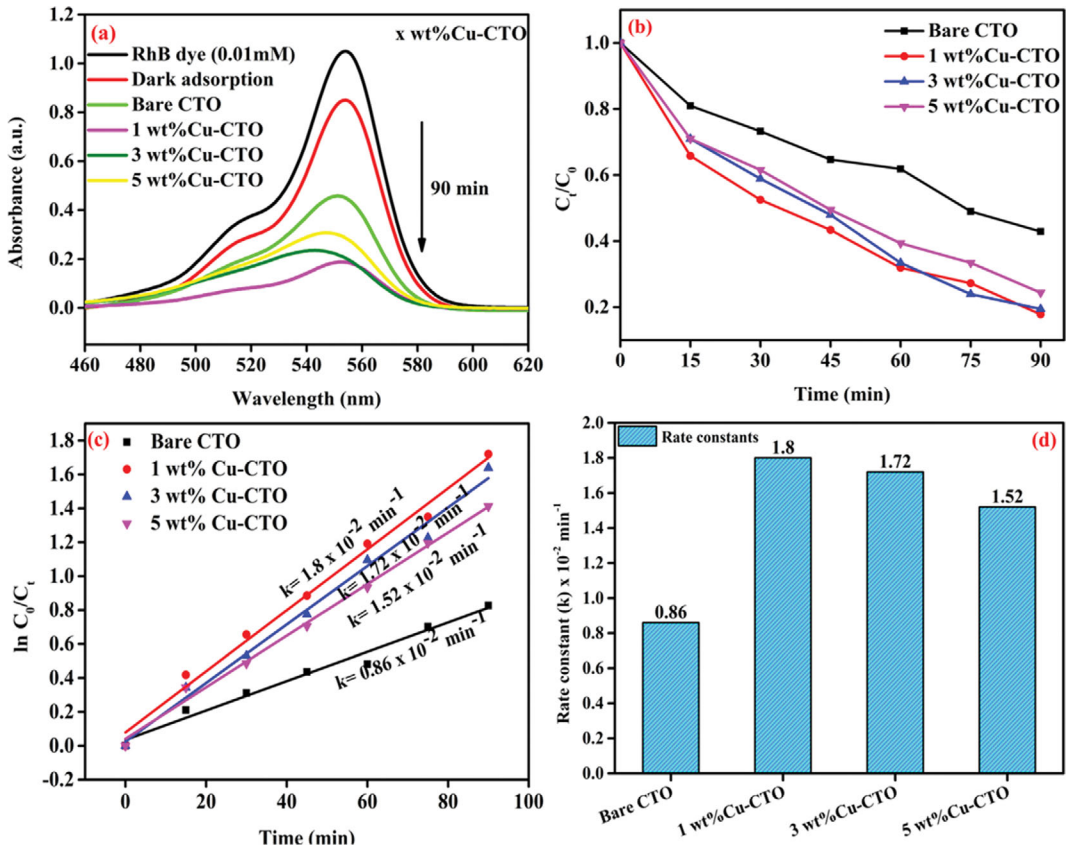

Fig. 10. (a) Comparative changes in absorption spectra of RhB dye degradation by different Cu-CTO catalysts after 90 min UV irradiation, ((b) and (c)) time course-kinetic plot, (d) their relative rate constants (k).

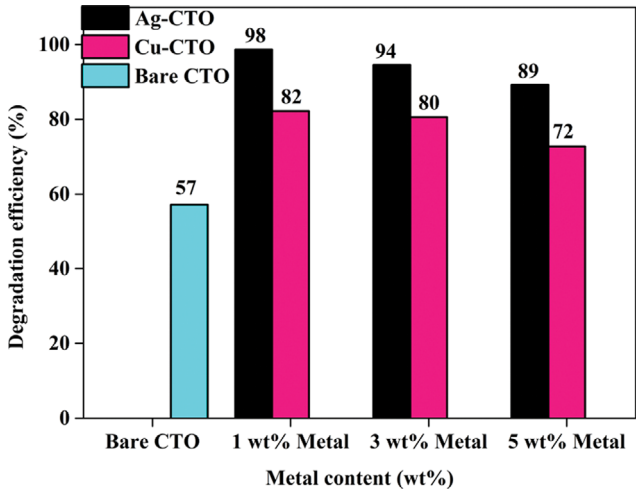

Fig. 11. Comparative photodegradation efficiency of different photocatalysts.

surface and then transfer them to oxygen molecule. Followed by increase in the formation of highly reactive hydroxyl (.OH-) radicals and superoxide radical anion (.O_2-), which can be used effectively for degradation of RhB. To further understand the improved behavior of CTO photoactivity, the CB (conduction band) and VB (valence band) potentials of CTO v/s (NHE) normal hydrogen electrode were determined based on its band gap by Eqs. (3)-(4).

$$E_{CB}=X-E_e-0.5E_g \quad (3)$$

$$E_{CB}=X-E_e+0.5E_g \quad (4)$$

where X is the absolute electronegativity of CTO (5.105 eV) [46]; E_e is the energy of free electrons on the hydrogen scale (4.5 eV), E_g is the band gap of CTO (2.99 eV). The CB and VB potentials were obtained as −0.89 V and +2.1 V vs NHE, respectively.

Comparative analysis of the co-catalytic effect imparted by Ag/Cu to $CaTiO_3$ photoactivity is presented in Fig. 11. The histogram clearly shows the differences in the degradation efficiency of RhB by various samples. 1 wt%Ag-CTO revealed the maximum RhB removal efficiency (98%) within 90 min. Since the amount of metal loading and the average particle size are almost the same in both the Ag and Cu deposited composites, the observed difference in the photoactivity of Ag/Cu-CTO catalysts can be elucidated on the basis of electronic properties like electron affinity and electronegativity and also the work function of the deposited metal. As it can be seen from Table 2, Ag metal, because of its high electron affinity (125.6 KJ/mol) and high electronegativity (1.93 on Pauling scale) value [47], acts as more efficient electron trap in comparison to the relatively lower values of Cu. Moreover, the lower work function of Ag metal (4.26 eV) than of Cu (4.93 eV), allows easy transference of the CB electrons of CTO to the Ag deposits. Further, the higher reduction potential of Ag^+ ions (0.79 V) accepts the electrons first from the CB while Cu^{+2} ions with lower reduction potential (0.33 V) get reduced afterwards.

Table 2. The electronic properties of Ag and Cu used as co-catalysts

Co-catalyst	Electron affinity (KJ/mol)	Electronegativity (Pauling)
Ag	125.6	1.93
Cu	118.4	1.90

As a result, much better separation of charges is achieved in the case of Ag loaded samples leading to superior degradation ability. Both the PL mesurements and bandgap analysis also support the observed degradation results. The lower bandgap value of (E_g=2.91 eV) as well much depressed PL intensity in case of 1 wt% Ag-CTO composites in contrast with the one deposited with Cu-CTO of (E_g=2.96 eV) acts as evidence for better efficiency of the Ag cocatalyst.

Furthermore, the lower degrading efficiency beyond 1 wt% deposition could be attributed to the fact that after exceeding this amount, the deposited Ag and Cu nanodots may cover the large portion of

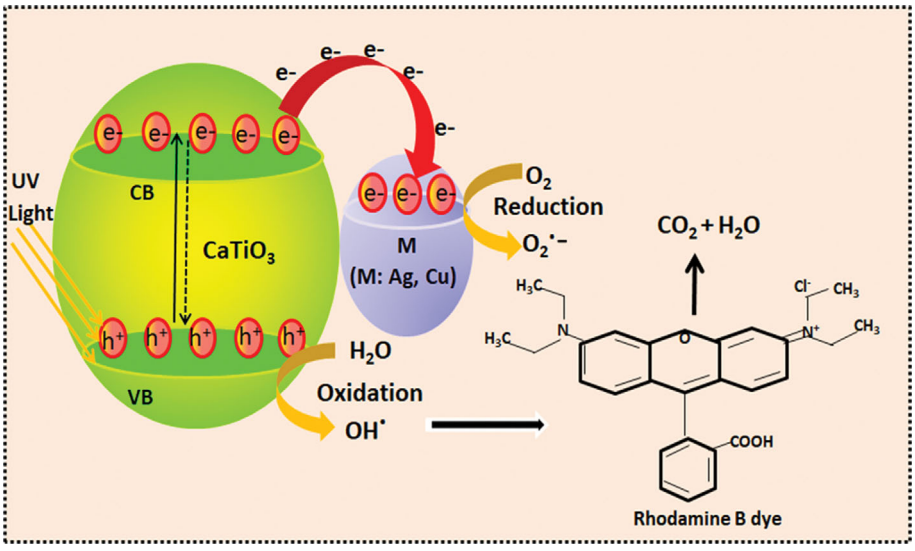

Scheme 3. Plausible mechanism of RhB degradation by Ag/Cu-$CaTiO_3$ nanocomposite under UV light irradiation.

CTO surface, leading to blockage of its many active sites and partial shielding of UV light absorption [48,49]. All these events probably reduce the number of photoinduced excitons (e^-/h^+). Furthermore, high amount of metal loading can also induce the agglomeration of metal particles, which in turn might be responsible for reducing the photoactivity. Thus, it is revealed that nature of metal and their amount also affects the photoactivity of $CaTiO_3$ for degrading RhB.

POSSIBLE PHOTOCATALYSIS MECHANISM

Scheme 3 illustrates the possible mechanism responsible for the degradation of RhB under UV light irradiation by the as-prepared catalysts. In CTO, during light illumination, the electrons get excited from the VB to the CB, with the simultaneous generation of holes (h^+) in the VB. Then the photoexcited electrons and holes react with adsorbed oxygen and water molecules to generate the reactive oxygen species, such as superoxide radical anions ($O_2^{\cdot-}$) and hydroxyl radicals. These strong oxidative species such as $O_2^{\cdot-}$ and $OH^{\cdot}$ radicals work together to further degrade or mineralize RhB [50].

Whereas, in case of Ag/Cu-CTO, owing to the lower redox potentials of Ag (+0.799 V vs. NHE) and Cu (+0.337 V vs. NHE) in comparison with the CB potential of CTO (−0.89 V), the photoexcited electrons can be easily transferred from CTO to Ag and Cu surface, which further speeds up the separation of the electron-hole pairs in CTO. Here, the deposited metals Ag, Cu act as electron sinks or traps for the photogenerated electrons migrated from CTO. This obstructs the immediate electron-hole recombination process. The overall reactions during photocatalysis under UV light with metal (M) deposited (CTO) photocatalyst are shown below [51]:

$$CTO + h\nu(UV) \rightarrow CTO\ (e^-_{CB} + h^+_{VB})$$
$$CTO\ (e^-_{CB}) + M\ (Ag, Cu) \rightarrow CTO\text{-}M\ (e^-)$$
$$CTO\text{-}M\ (e^-) + O_2 \rightarrow CTO\text{-}M + \cdot O_2^-$$
$$h^+_{VB} + OH^- \rightarrow \cdot OH$$
$$\cdot O_2^- + 2H^+ \rightarrow 2\cdot OH$$
$$\cdot OH + RhB \rightarrow \text{decomposed product}$$

CONCLUSION

We studied the effect of nature and amount of metal deposited on $CaTiO_3$ for its enhanced activity in degrading RhB dye under UV light irradiation. A series of Ag/Cu-CTO nanocomposites with varying wt% (1, 3 and 5) of Ag, Cu were synthesized by photodeposition method. Their photocatalytic activity for the degradation of Rhodamine B was found to be dramatically higher than that of bare CTO. Both Ag and Cu deposition promoted enlarged photoactivity by shifting the absorption edges towards longer wavelengths with reduced bandgaps and suppressing the charge carrier (electron-hole pairs) recombination probability, as confirmed by UV-DRS and PL spectroscopy, respectively. Optimal Ag and Cu loading (1 wt% in the present case) ensures the maximum degradation, whereas the rates were gradually reduced with higher metal loading. Also, in comparison to Cu, much superior reaction rates= $4.5\times10^{-2}\ min^{-1}$ were achieved by deposition of Ag onto CTO. So, based on the experimental results, Ag was found to be a promising co-catalyst for $CaTiO_3$. In addition, the as-prepared composites not only show enhanced activity under UV light, but also possesses strong absorption in the visible light region as seen by the UV-DRS plot. Further, the work of exploring their photocatalytic activity under visible and solar irradiation is currently under progress. This study will enlighten the usage of these materials applications for developing other visible-light responsive perovskites photocatalysts with high photocatalytic activity in various environmental and energy issues.

ACKNOWLEDGEMENTS

The authors are highly thankful to SAI labs, TIET Patiala for XRD, SEM-EDS and elemental mapping analysis and we also acknowledge the TEM facility, funded by a TPF Nanomission, GOI project at Centre for Nano and Soft Matter Sciences, Bengaluru for TEM analysis.

CONFLICTS OF INTEREST

The authors declare that there are no conflicts of interest regarding the publication of this manuscript.

FUNDING

This research did not receive any specific grant from funding agencies in the public, commercial, or not-for-profit sectors.

SUPPORTING INFORMATION

Additional information as noted in the text. This information is available via the Internet at http://www.springer.com/chemistry/journal/11814.

REFERENCES

1. M. Kurian, *Clean. Eng. Technol.*, **2**, 100090 (2021).
2. A. G. Gutierrez-Mata, S. Velazquez-Martínez, A. Álvarez-Gallegos, M. Ahmadi, J. A. Hernández-Pérez, F. Ghanbari and S. Silva-Martínez, *Int. J. Photoenergy*, **2017**, 1 (2017).
3. N. F. Atta, A. Galal and E. H. El-Ads, *Perovskite Materials - synthesis, characterization, properties, and applications*, IntechOpen, London, UK (2016).
4. E. A. R. Assirey, *Saudi Pharm. J.*, **27**, 817 (2019).
5. X. Huang, G. Zhao, G. Wang and J. T. S. Irvine, *Chem. Sci.*, **9**, 3623 (2018).
6. A. Kumar, A. Kumar and V. Krishnan, *ACS Catal.*, **10**, 10253 (2020).
7. P. Kanhere and Z. Chen, *Molecules*, **19**, 19995 (2014).
8. V. H. Nguyen, H. H. Do, T. Van Nguyen, P. Singh, P. Raizada, A. Sharma, S. S. Sana, A. N. Grace, M. Shokouhimehr, S. H. Ahn, C. Xia, S. Y. Kim and Q. Van Le, *Sol. Energy*, **211**, 584 (2020).
9. E. Jiang, L. Yang, N. Song, X. Zhang, C. Liu and H. Dong, *J. Colloid Interface Sci.*, **576**, 21 (2020).
10. J. Pan, Z. Jiang, S. Feng, C. Zhao, Z. Dong, B. Wang, J. Wang, C.

Song, Y. Zheng and C. Li, *Int. J. Hydrogen Energy*, **43**, 19019 (2018).
11. J. Han, Y. Liu, F. Dai, R. Zhao and L. Wang, *Appl. Surf. Sci.*, **459**, 520 (2018).
12. M. Passi and B. Pal, *Powder Technol.*, **388**, 274 (2021).
13. Y. Yan, H. Yang, Z. Yi, R. Li and T. Xian, *Solid State Sci.*, **100**, 106102 (2020).
14. J. Zhuang, Q. Tian, S. Lin, W. Yang, L. Chen and P. Liu, *Appl. Catal. B Environ.*, **156**, 108 (2014).
15. Y. Yan, H. Yang, Z. Yi, T. Xian and X. Wang, *Environ. Sci. Pollut. Res.*, **26**, 29020 (2019).
16. S. Lanfredi, J. Matos, S. R. da Silva, E. Djurado, A. S. Sadouki, A. Chouaih, P. S. Poon, E. R. P. González and M. A. L. Nobre, *Appl. Catal. B Environ.*, **272**, 118986 (2020).
17. K. V. Yatish, H. S. Lalithamba, R. Suresh and H. K. E. Latha, *Renew. Energy*, **147**, 310 (2020).
18. H. Yang, C. Han and X. Xue, *JES*, **26**, 1489 (2014).
19. X. Chen, L. Di, H. Yang and T. Xian, *J. Ceram. Soc. Japan*, **127**, 221 (2019).
20. B. Deng, P. Si, L. Bauman, J. Luo, M. Rao, Z. Peng, T. Jiang, G. Li and B. Zhao, *J. Clean. Prod.*, **244**, 118598 (2019).
21. L. Bai, Q. Xu and Z. Cai, *J. Mater. Sci. Mater. Electron.*, **29**, 17580 (2018).
22. L. H. Oliveira, A. P. De Moura, F. A. La Porta, I. C. Nogueira, E. C. Aguiar, T. Sequinel, I. L. V. Rosa, E. Longo and J. A. Varela, *Mater. Res. Bull.*, **81**, 1 (2016).
23. R. Wang, S. Ni, G. Liu and X. Xu, *Appl. Catal. B Environ.*, **225**, 139 (2018).
24. L. H. Oliveira, J. Savioli, A. P. De Moura, I. C. Nogueira, M. S. Li, E. Longo, J. A. Varela and I. L. V. Rosa, *J. Alloys Compd.*, **64**, 265 (2015).
25. C. Science, G. Jiajian, F. Gu and Z. Zhong, *Catal. Sci. Technol.*, **3**, 490 (2013).
26. K. Shimura and H. Yoshida, *Energy Environ. Sci.*, **3**, 615 (2010).
27. C. Han, J. Liu, W. Yang, Q. Wu, H. Yang and X. Xue, *J. Photochem. Photobiol. A Chem*, **322**, 1 (2016).
28. J. Lin, J. Hu, C. Qiu, H. Huang, L. Chen, Y. Xie, Z. Zhang, H. Lin and X. Wang, *Catal. Sci. Technol.*, **9**, 336 (2019).
29. Z. Jiang, J. Pan, B. Wang and C. Li, *Appl. Surf. Sci.*, **436**, 519 (2018).
30. Y. Liu, J. Pan, H. Li, W. Ou, S. Li, W. Zhao, J. Wang, C. Song, Y. Zheng and C. Li, *J. Alloys Compd.*, **811**, 152067 (2019).
31. T. Xian, H. Yang and Y. S. Huo, *Phys. Scr.*, **89**, 115801 (2014).
32. A. Kumar, S. Kumar, A. Bahuguna, A. Kumar, V. Sharma and V. Krishnan, *Mater. Chem. Front.*, **1**, 2391 (2017).
33. A. Kumar, C. Schuerings, S. Kumar, A. Kumar and V. Krishnan, *Beilstein J. Nanotechnol.*, **9**, 671 (2018).
34. Y. S. Fu, J. Li and J. Li, *Nanomaterials*, **9**, 359 (2019).
35. A. Shawky, M. Alhaddad, K. S. Al-Namshah, R. M. Mohamed and N. S. Awwad, *J. Mol. Liq.*, **304**, 3 (2020).
36. A. Alzahrani, D. Barbash and A. Samokhvalov, *J. Phys. Chem. C.*, **120**, 19970 (2016).
37. S. W. Lee, L. M. Lozano-Sánchez and V. Rodríguez-González, *J. Hazard. Mater.*, **263**, 20 (2013).
38. Y. Yan, H. Yang, Z. Yi, R. Li and X. Wang, *Micromachines*, **10**, 1 (2019).
39. S. Bhardwaj and B. Pal, *Adv. Powder Technol.*, **29**, 2119 (2018).
40. H. Zhang, G. Chen, Y. Li and Y. Teng, *Int. J. Hydrogen Energy*, **35**, 2713 (2010).
41. J. Kaur and B. Pal, *Environ. Sci. Pollut. Res.*, **20**, 3956 (2013).
42. W. Dong, Q. Bao, X. Gu and G. Zhao, *J. Ceram. Soc. Jpn.*, **123**, 643 (2015).
43. V. D. Doan, B. A. Huynh, T. D. Nguyen, X. T. Cao, V. C. Nguyen, T. L. H. Nguyen, H. T. Nguyen and V. T. Le, *J. Nanomater.*, **2020**, 8492016 (2020).
44. Y. Zhai, Y. Ji, G. Wang, Y. Zhu, H. Liu, Z. Zhong and F. Su, *RSC Adv.*, **5**, 73011 (2015).
45. J. Liqiang, Q. Yichun, W. Baiqi, L. Shudan, J. Baojiang, Y. Libin, F. Wei, F. Honggang and S. Jiazhong, *Sol. Energy Mater. Sol. Cells*, **90**, 1773 (2006).
46. X. Yan, X. Huang, Y. Fang, Y. Min, Z. Wu, W. Li and J. Yuan, *Int. J. Electrochem. Sci.*, **9**, 5155 (2014).
47. S. Oros-Ruiz, R. Zanella and B. Prado, *J. Hazard. Mater.*, **26**, 328 (2013).
48. A. Gnanaprakasam, V. M. Sivakumar and M. Thirumarimurugan, *Water Sci. Technol.*, **74**, 1426 (2016).
49. B. Luo, D. Xu, D. Li, G. Wu, M. Wu, W. Shi and M. Chen, *ACS Appl. Mater. Interfaces*, **7**, 17061 (2015).
50. P. Fageria, S. Gangopadhyay and S. Pande, *RSC Adv.*, **4**, 24962 (2014).
51. Ş. Ş. Türkyılmaz, N. Güy and M. Özacar, *J. Photochem. Photobiol. A Chem.*, **341**, 39 (2017).